

Particle in cell simulation on mode conversion of Saturn's 20 kHz narrowband radio emission

Zhoufan Mu¹, Yao Chen^{1,2,3}, Tangmu Li¹, Sulan Ni⁴, Zilong Zhang^{2,3}, and Hao Ning¹

¹Institute of Frontier and Interdisciplinary Science, Shandong University, Qingdao, Shandong 266237, PR China

²Shandong Key Laboratory of Space Environment and Exploration Technology, Shandong University, Shandong 264209, PR China

³Institute of Space Sciences, Shandong University, Shandong 264209, PR China

⁴School of Physics and Electronic Information, Yantai University, Yantai 264005, PR China

Key Points:

- We conduct fully-kinetic 2D3V particle-in-cell simulation of the mode conversion process underlying the Saturn's 20 kHz narrowband radiation.
- We use the wave-pumping method to initiate the Z-to-O mode conversion induced by the density gradient.
- We identify the Z mode-converted electromagnetic radiation and estimate the mode conversion rate to be 10-20%.

Corresponding author: Yao Chen, yaochen@sdu.edu.cn

Abstract

The Z-to-O mode conversion at the density gradient is the prevailing mechanism of narrowband (NB) radio emission in planetary magnetosphere. Most previous numerical models were for NB emission observed in the Earth magnetosphere, using the cold plasma fluid approximation that excluded any kinetic effect. Here we investigate the Z-to-O conversion process underlying the Saturn’s 20 kHz NB emission, using the fully-kinetic and electromagnetic particle-in-cell (PIC) simulation. We simulate the whole process starting from the pumping of the Z mode, to its propagation and reflection, and further conversion into the O mode radiation. The energy conversion rate of the Z-to-O process is estimated to be 10-20%. This provides the first quantitative estimate of such rate with PIC simulations.

Plain Language Summary

Saturn emits 20 kHz narrowband radio signals in regions where plasma density changes abruptly. Using advanced computer simulations, we discovered how trapped waves can convert to radio waves that can escape into space: When these “trapped waves” encounter areas of increasing density—much like light propagating into lens—their path curves till they align with the magnetic field. This alignment allows them to transform into radio signals that can be detected on Earth. Our key finding is that 10-20% of the trapped wave energy converts into these escaping signals. This explains Saturn’s narrowband radio emissions and helps scientists decode similar signals observed near other planets by missions like Cassini and Juno, improving our understanding of planetary space environments.

1 Introduction

Plasma emission refers to coherent radiation from plasmas at frequencies close to the fundamental plasma frequency (ω_{pe}) and/or its harmonics (Ginzburg & Zhelezniakov, 1958). Two processes have been proposed to account for such emissions. The first one is the standard beam-driven plasma emission that is a nonlinear and multi-step process starting from the bump-on-tail instability driven by beam of energetic electrons. The instability excites Langmuir waves which interact with density fluctuations or the ion acoustic wave non-linearly to generate the escaping O mode wave (i.e., the fundamental branch). These Langmuir waves also interact with the induced backward-propagating Langmuir waves to generate the harmonic radiation at $2\omega_{pe}$ (Ginzburg & Zhelezniakov, 1958; Melrose, 1980; Cairns & Melrose, 1985; Robinson et al., 1994a, 1994b)

The second plasma emission process is given by the mode conversion from Z to O at density gradient. Such process has been generally used to explain the narrowband (NB) radiation observed from planets, or the nonthermal continuum (NTC) radiation observed in the Earth’s magnetosphere. Gurnett (1975) were the first to report the latter radiation using IMP-6 data. Subsequent observations revealed similar emissions, which have been termed as the NB radiation, from the magnetospheres of Saturn, Jupiter and its moon Ganymede (Kurth et al., 1981, 1997, 2022; Gurnett, 1975; Gurnett et al., 1981, 1983, 1996; Grimald et al., 2008; Grimald & Santolík, 2010). Such radiation shares the following common characteristics (Menietti et al., 2012; Décréau et al., 2015): (1) having multiple harmonic structures; (2) being closely associated with intense Upper Hybrid (UH) or Z mode (i.e., the slow extraordinary mode); (3) originating from regions with steep density gradients such as plasma sheet boundaries or planetary rings.

Jones (1980, 1987) proposed the Z-to-O mode conversion process in density gradient to explain the plasma emissions from planets. This process has three stages: (1) High-energy electrons excite multiple UH oscillations with large wavenumbers through

the double plasma resonance process along the structure with density gradient; (2) As these UH oscillations propagate into denser regions, their wavenumber decreases till they evolve into the electromagnetic Z mode; (3) The Z mode gets reflected at a certain location. The reflected Z mode propagates into the so-called Ellis window when its frequency ω is close to the local plasma oscillation frequency ω_{pe} (G. Ellis, 1956; G. R. A. Ellis, 1962). Within the window both Z and O modes propagate parallel to the background magnetic field with identical frequency and wavenumber. This leads to the mode conversion process. Recent studies also employed the Z-to-O mode conversion to explain solar radio bursts (Sakai et al., 2005; Willes & Cairns, 2001; Krafft & Volokitin, 2024; Krafft & Savoini, 2024; Krafft et al., 2024).

Figure 1 from Ye et al. (2009) displays the 20 kHz NB and the associated electrostatic disturbances detected by Cassini-RPWS while crossing the boundary layer of Saturn's plasma sheath on 04/01/2008. Electrostatic UH signals showed a sharp increase in frequency, indicating a density gradient at the sheath boundary. According to Ye et al. (2009), the radiation has multiple bands with left-handed polarization, within 3 to 70 kHz. They also demonstrated that the weak NB signals are linked to the strong electrostatic source, indicating that the NB radiation originates from the intense UH/Z mode waves. According to the intensity ratio indicated by the color scale in Figure 1, the energy conversion rate from UH/Z mode to NB radiation is 1%. These observations support the NB origin of the UH/Z-to-O conversion process due to the density gradient (Ye et al., 2009, 2010; Menietti et al., 2009).

Kim et al. (2007, 2008) simulated mode conversion in warm plasma under typical solar wind conditions, using an electron-fluid model with density gradient. Their study focused on the conversion of Langmuir waves into electromagnetic (X/O mode) radiation, and estimated the maximum efficiency of mode conversion from the incident Langmuir wave to the electromagnetic wave. Kalaei et al. (2009) injected UH waves obliquely to the magnetic field with a 2D fluid simulation, setting the width of the density gradient to be 5 times the wavelength of the UH mode. They showed the occurrence of the Z-to-O mode conversion, and estimated the Poynting flux ratio of O mode to initial UH mode to be 50%. In a series of studies, the authors investigated how different propagation angles and density gradient widths affect the conversion efficiency (Kalaei & Kato, 2014, 2020).

PIC simulations self-consistently solve the equations of particle motion and those of the electromagnetic fields, thus the method has been used to verify the nonlinear plasma emission process (Thurgood & Tsiklauri, 2015; Henri et al., 2019; Chen et al., 2022; Zhang et al., 2022). For instance, Zhang et al. (2022) conducted PIC simulations within a uniform domain with a large number of macroparticles, and estimated the conversion rate of energy from the beam of energetic electrons to be $\sim 5 * 10^{-6}$ for the fundamental emission and $\sim 4 * 10^{-5}$ for the harmonic emission. Studies by Krafft and Savoini (2021) have investigated the effect of density fluctuations on the plasma emission process. They concluded that the ratio of harmonic emission energy to Langmuir wave turbulence energy exceeds $\sim 10^{-3}$ in inhomogeneous plasma and $\sim 10^{-4}$ in homogeneous plasma, and found that density fluctuations tend to enhance the growth rates of harmonic emission.

Horký et al. (2018); Horký and Omura (2019) conducted PIC simulations of the NTC radiation under conditions of the Earth's magnetosphere by injecting ring-distributed energetic electrons into regions of increasing density. They suggested the obtained O mode radiation originate from the conversion of the ring-excited Bernstein mode due to the density gradient, though no obvious signature of electromagnetic waves was observed in the post-conversion dispersion diagram (see Figure 7 of Horký et al. (2018)). This implicates the necessity of further study on the mode conversion process induced by density gradient.

In this article, we use fully kinetic and electromagnetic PIC simulations to study the Z-to-O mode conversion process induced by density gradient. We also estimate the energy conversion rate of the process. In Section 2 we present the numerical method and parameter setup. The simulation result is presented in Section 3, and Section 5 and 4 present our conclusion and discussion, respectively.

2 Numerical method and parameter setup

We used the Vector-PIC (vPIC) open-source code released by the Los Alamos National Laboratory (Bowers et al., 2008, 2009). The code applies a second-order, explicit leapfrog algorithm to resolve the particle motion and a second-order finite-difference time-domain solver to solve the full Maxwellian equations of the electric-magnetic fields. The simulations are 2D3V, i.e., with two spatial dimensions in the XOZ plane and three velocity components, with periodic boundary conditions.

We set the thermal velocity (v_{the}) of both electrons and protons to be $0.01c$ (Menietti et al., 2019). We set the background magnetic field along the z-axis (i.e., the parallel direction, $\vec{B}_0 = B_0 \hat{e}_z$), and the wave vector $\vec{k} = k_x \hat{e}_x + k_z \hat{e}_z$, where $k_{\parallel} = k_z, k_{\perp} = k_x$. The simulation domain spanned $L_x = L_z = 18 c/\Omega_{ce}$, with a grid size of 2048×2048 . We set the time step to be $\Delta t = 0.0217 \omega_{pe}^{-1}$ and ran the simulation for $4000 \omega_{pe}^{-1}$. We used the realistic proton-to-electron mass ratio ($m_p/m_e = 1836$), and employed 1000 particles of each species in each grid. The total number of particles is 8.4×10^9 .

According to Figure 1, the ratio ω_{pe}/Ω_{ce} is 5. We determine the O mode radiation frequency from the figure to be $\omega = 5.03 \Omega_{ce}$. Following Kalaei et al. (2009), we solved the cold-plasma magnetoionic dispersion relation together with the Snell's law (see Figure C1). The density gradient is parallel to magnetic field (\vec{B}), so both ω_{pe} and the refractive index N vary perpendicular to \vec{B} . According to the Snell's law, both θ (the angle between \vec{k} and \vec{B}) and k_x vary with N , while k_z remains constant. The Z mode propagates into the Ellis window with $\omega_{pe} \sim \omega$, where the mode conversion occurs.

Figure 2 presents the setup of the density gradient that is perpendicular to $B_0 \cdot e_z$. We set ω_{pe} increases from $5 \Omega_{ce}$ to $5.2 \Omega_{ce}$ over a width of $5.6 c/\Omega_{ce}$. With the method presented in Appendix A, we deduced the initial wavenumber of the Z mode to be $k_0 = 6.0 \Omega_{ce}/c$, and its propagation angle $\theta_0 = 70.6^\circ$. With the method presented in Appendix B, we pumped the Z mode into the uniform region (blue lines in Figure 2). According to the linear theory of cold-plasma, the Z mode will get reflected at the return point (green line) where $\omega_r = 5.13 \Omega_{ce}$, it partially converts to the O mode when it reaches the Ellis window (red line) where $\omega_c = 5.03 \Omega_{ce}$.

3 PIC simulations of mode conversion

This section presents the complete process of mode conversion, starting from the pumping of Z mode to its further reflection and mode-conversion. According to Figure 3, we pumped the Z mode in the uniform region with $k = 6.0 \Omega_{ce}/c$, $\omega = 5.03 \Omega_{ce}$, and $\theta_0 = 70.6^\circ$. We split the whole process into four stages:

- 1) From 0 to $400 \omega_{pe}^{-1}$ and then to $1300 \omega_{pe}^{-1}$, the Z mode propagates from the uniform to the nonuniform region, within the latter region θ_0 decreases from 70° to $\sim 30^\circ$.
- 2) From 1300 to $1800 \omega_{pe}^{-1}$, the upper part of the Z mode is reflected at the return zone, where $\theta \sim 30^\circ$. Then it moves into the less-denser region with decreasing θ . When $\theta \sim 0$ or the mode propagates almost parallel to \vec{B}_0 , it reaches the conversion zone while propagates into the uniform region.
- 3) From 1800 to $2000 \omega_{pe}^{-1}$, with the continuous entry of the Z mode into the return zone, an interference signal appears with the incident and reflected Z modes. Ac-

cording to Figure 3, as more and more Z mode gets reflected, we observed continuous enhancement of parallel and quasi-parallel propagating waves, as a result of continuous mode conversion.

- 4) From 2000 to 2700 ω_{pe}^{-1} , all the Z mode is reflected around the return zone. After that, the signal of the reflected Z mode dominates over that of the O mode (not shown here). In the following text, we analyzed the changes in wave number and energy during the wave mode conversion process, and calculated the conversion efficiency.

3.1 The mode conversion process

A small-amplitude plane wave obeys the Snell's law that means k_{\perp} of the pumped Z mode decrease while k_{\parallel} remains constant. The linear theory (see Appendix A) predicts the reflection take place at $\omega_r = 5.13 \Omega_{ce}$ where θ jumps from $\sim 30^\circ$ to $\sim -30^\circ$. The reflection occurs with a spatially-extended return zone with a length of $\sim 1 c/\Omega_{ce}$.

Figure 4 illustrates the wave intensity maps of electromagnetic (EM) fields in the wave-vector space, highlighting the wavenumber change of Z mode. Panel (a) shows the initial Z mode propagation in the uniform region from 0 to 400 ω_{pe}^{-1} , both k and θ remain fixed to the prescribed values. In Panels (b) and (c), E_x weakens with decreasing θ , while E_z dominates for $k_x \sim 0$. Panel (d) for the post-conversion stage manifests the strong signal of the reflected Z mode, along with a weaker signal of parallel-propagating O mode. Figure 5 presents the $\omega-k$ dispersion relations for different propagation angles. Panel (e) shows a parallel-propagating O mode emerging during 1600–2400 ω_{pe}^{-1} , with the E_x/E_z ratio consistent with the wave signatures observed in Figure 4. Appendix C details the mode identification method used to deduce the occurrence of the Z-to-O mode conversion.

3.2 Energy evolution and rate of mode conversion

Figure 6 displays the energy profiles of the six components of the EM field, normalized to their corresponding initial values, within the full domain (left) and the uniform region (right). During the propagation of the Z mode toward the density gradient (0 to 1700 ω_{pe}^{-1}), E_x and total energy decrease throughout the domain. During the phase of mode conversion (1700 to 2100 ω_{pe}^{-1}), we observed E_x weakening, E_z strengthening, and E_y remaining fixed in energy. Again, this is in line with the occurrence of mode conversion. From 2100 to 2900 ω_{pe}^{-1} , the Z mode reflects and gradually dissipates. In the uniform region, the Z mode is dominated by the E_x component before 1700 ω_{pe}^{-1} . From 1700 to 2100 ω_{pe}^{-1} , E_z increases significantly from -1.8×10^{-5} to -1.2×10^{-5} , again, agreeing with the Z-to-O mode conversion. Figure 6 (left) shows the decrease of the total energy W of the pumped Z mode as it propagates. After 1300 ω_{pe}^{-1} , when the Z mode reaches the return zone, W remains nearly constant, while E_x gets weaker, E_y and E_z get stronger in energy. This indicates a reduction of θ of the Z mode, as shown in Figure 3.

We evaluated the wave energy within the black-dashed region marked in Figure 3. Figure 6 reveals a decrease in Z mode energy during 0–1000 ω_{pe}^{-1} , indicating energy transfer from electromagnetic fields to plasma particles through wave-particle interactions. This energy decline ceased after 1000 ω_{pe}^{-1} . Consequently, we measured the pre-conversion Z mode energy (W_E^Z) at 1300 ω_{pe}^{-1} , while the post-conversion O mode energy (W_E^O) at 2000 ω_{pe}^{-1} . The conversion efficiency η was calculated as the ratio of W_E^O to W_E^Z , $\eta = (W_E^O) / (W_E^Z) = 17.5\%$.

4 Discussion

According to Figure 3, part of the downward-propagating Z mode gets reflected back into the domain due to the periodic boundary condition. This gets mixed with the

newly-converted O mode signal and affects our estimates of the energy budget. Further studies can improve this by using a larger domain. Previous PIC simulations of nonlinear plasma emission processes (Krafft & Savoini, 2021; Chen et al., 2022; Zhang et al., 2022), show that only $\sim 10^{-3} - 10^{-4}$ of the energy of the beam-driven Langmuir turbulence can convert into escaping radiation. In our simulation, we started from directly pumping Z mode with appropriate conditions into the system, this explains why the mode conversion rate (10-20%) obtained here is much larger.

Saturn's NB emissions consist of two major components, one is at 20 kHz and the other is at 5 kHz. Both are attributed to the conversion of the Z mode waves upon density gradient. Yet, their source conditions exhibit significant differences in ω_{pe}/Ω_{ce} . For the 20 kHz one, ω_{pe}/Ω_{ce} reaches ~ 5 , while for the 5 kHz one ω_{pe}/Ω_{ce} is $\lesssim 1$ (Ye et al., 2010). In addition, the conversion frequency for the 20 kHz one is $\sim \omega_{pe}$ and that for the 5 kHz one is $\sim \Omega_{ce}$. This may indicate that the two NB radiation originate from different conversion process. Further simulations are demanded to examine such difference.

The mechanisms or the features or the observational characteristics of NB radiations vary across planets due to distinct source regions and plasma parameters. Table 1 collects published parameters for NB from Ganymede near its magnetopause ($\sim 5.4 R_G$), from Earth near its plasmapause and from Jupiter at various sites: the extensive region (5-25 R_J) away from the plasma disk (Reiner et al., 1993; Boudouma et al., 2024), the day-side of the magnetosphere (Gurnett et al., 1983) and near the Jovian magnetopause (Kaiser et al., 1992). Except for Saturn's 5 kHz NB radiation, ω_{pe}/Ω_{ce} is always $\lesssim 1$ (Kurth et al., 1997; Gurnett et al., 1983; Grimald et al., 2008; Ye et al., 2009; Wu et al., 2021). Further studies can explore the difference of conversion on different planets.

5 Conclusions

We present the fully kinetic electromagnetic PIC simulations of the Z-to-O mode conversion induced by density gradient, using physical conditions in line with the Saturn's 20 kHz NB radiation. We started the simulation by pumping the Z mode wave with prescribed conditions into the domain, and simulated its further reflection and conversion into the quasi-parallel-propagating O mode emission. The simulation results agree with the predictions given by the linear magnetoionic wave theory of cold plasma and the Snell's law. We estimated the rate of energy conversion from Z mode to O mode to be 10-20%.

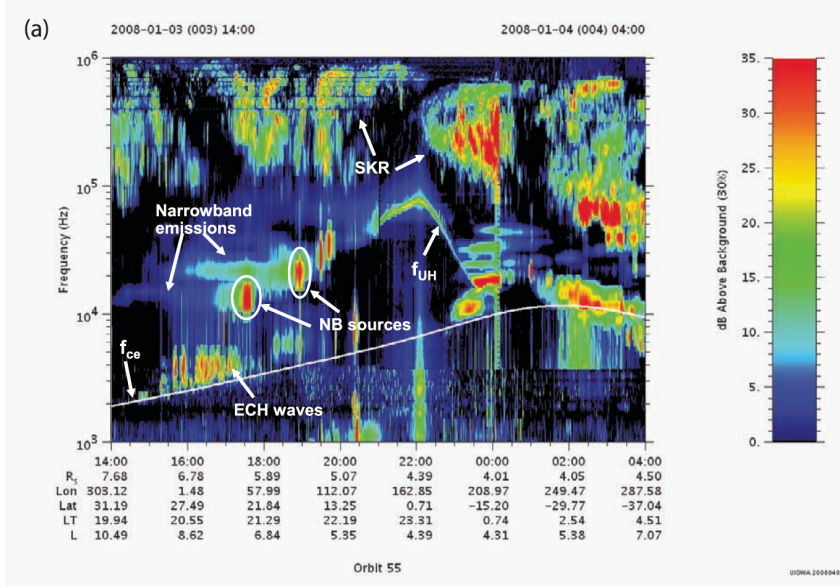


Figure 1. Spectrogram of the Cassini-RPWS observations on 04/01/2008 during its crossing of the source region of the 20 kHz NB. The detection of Saturn Kilometric Radiation (SKR), Electron Cyclotron Harmonics (ECH), narrowband radiation (NB) and their sources are annotated in white. The white line represents the electron cyclotron frequency f_{ce} . The x-axis corresponds to the Cassini observations time period, radial distance (R_s), longitude (Lon), latitude (Lat), local time (LT) and L-shell value (L). The y-axis corresponds to the Cassini-RPWS frequency channels from 1 kHz to 1 MHz, distributed on a logarithmic scale. This Figure is adapted from Figure 1 of Ye et al. (2009).

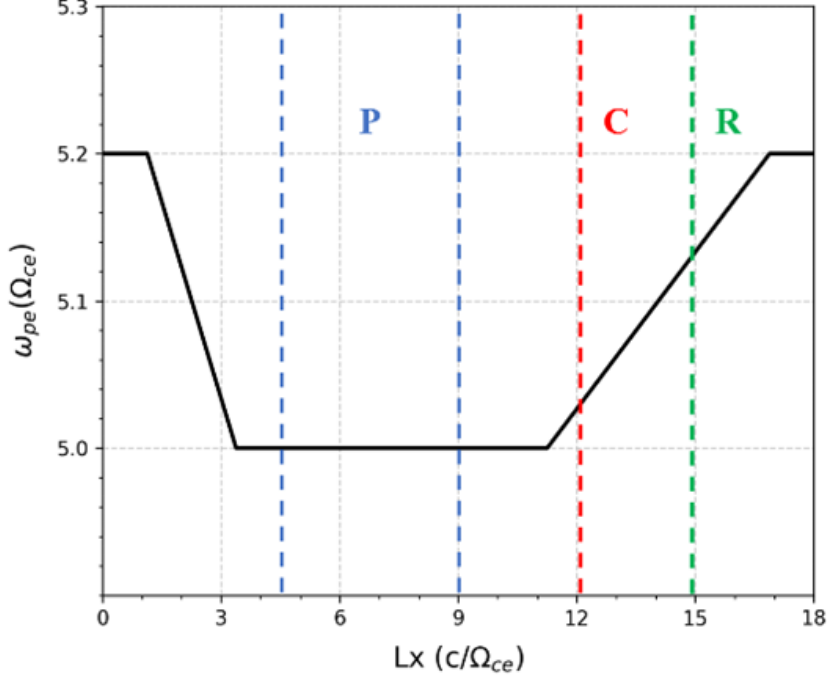


Figure 2. Slice of background plasma density along the L_x direction (normalized by c/ω_{pe}), expressed as plasma frequency ω_{pe}/Ω_{ce} . The density gradient increase from 5.0 to 5.2 Ω_{ce} . Two blue lines demarcate the Z mode pumping zone “P” ($L_x = 4.5 - 9 c/\Omega_{ce}$). Green line marks the theoretical return zone “R” ($\omega_{pe} = 5.13 \Omega_{ce}$) and red line marks the Z-to-O mode conversion zone “C” ($\omega_{pe} = 5.03 \Omega_{ce}$).

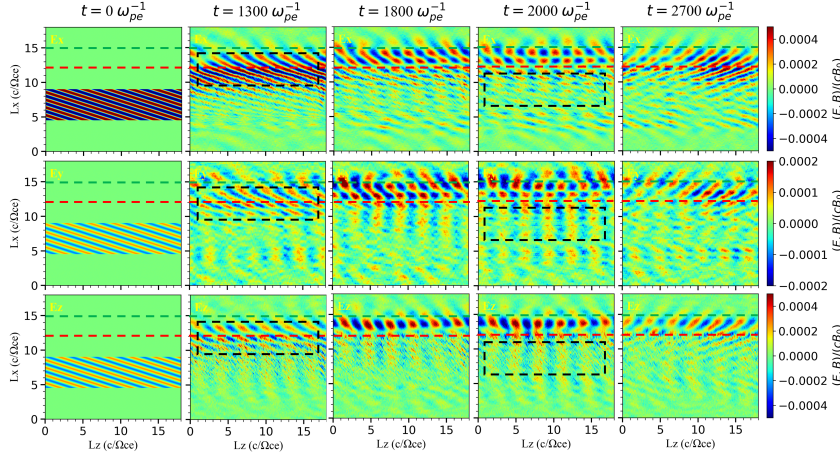


Figure 3. Snapshot of electric field components (E_x, E_y, E_z) during mode conversion across five sequential phases: (1) initial state of pumped Z mode ($t = 0 \omega_{pe}^{-1}$); (2) propagation of Z mode in density gradient ($t = 1300 \omega_{pe}^{-1}$); (3) reflection of Z mode in return zone ($t = 1800 \omega_{pe}^{-1}$); (4) emergence of O mode ($t = 2000 \omega_{pe}^{-1}$); (5) post-conversion stage ($t = 2700 \omega_{pe}^{-1}$). Red and green lines mark conversion and return zones, black dashed box indicates the energy-calculation region (section 3.2).

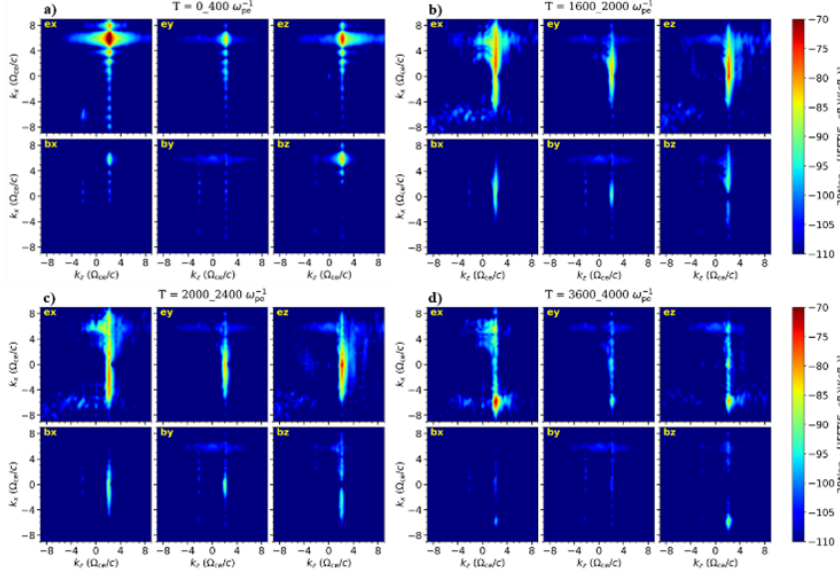


Figure 4. Wave intensity maps of EM fields ($E_x, E_y, E_z, B_x, B_y, B_z$) in the wave-vector space ($k_x - k_z$), with wave number units of Ω_{ce}/c . Panel (a) corresponds to the initial Z mode in the uniform region ($0 - 400 \omega_{pe}^{-1}$); Panels (b) and (c) correspond to the Z mode propagation in the non-uniform region (respectively $1600 - 2000 \omega_{pe}^{-1}$ and $2000 - 2400 \omega_{pe}^{-1}$); Panel (d) corresponds to the post-conversion stage with the reflected Z mode and the quasi-parallel O mode near $k_x \sim 0$ (after $3600 \omega_{pe}^{-1}$).

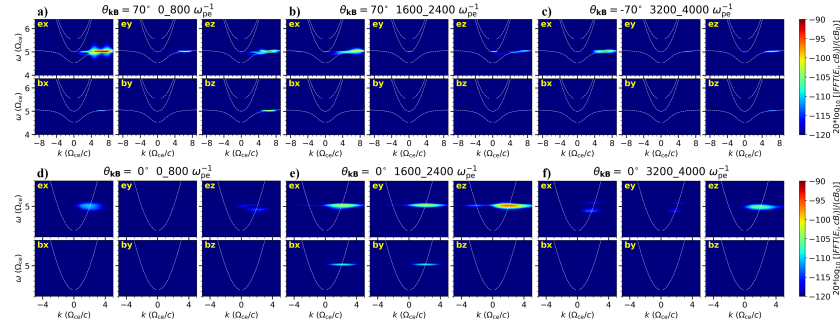


Figure 5. Dispersion relations in uniform region for $\theta = 70^\circ |k_{max}| = 9 \Omega_{ce}/c$ (top) and $\theta = 0^\circ |k_{max}| = 5 \Omega_{ce}/c$ (bottom). Top row shows three temporal phases: (a) initial stage ($0 - 800 \omega_{pe}^{-1}$); (b) mode conversion ($1600 - 2400 \omega_{pe}^{-1}$); (c) post-conversion ($3200 - 4000 \omega_{pe}^{-1}$). Bottom row shows quasi-parallel propagation of mode waves at corresponding times. White curves represent the theoretical dispersion in the uniform region.

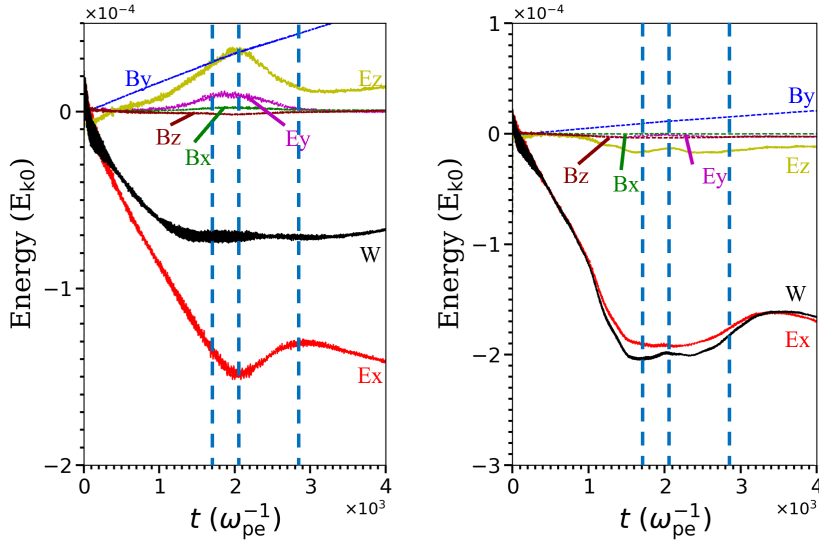


Figure 6. Temporal evolution of EM field components ($E_x, E_y, E_z, B_x, B_y, B_z$) and total EM energy (W), normalized to their respective initial values. Left panel shows the full solution domain, and right panel shows the uniform region. Blue dashed lines demarcate four temporal phases: (1) Z mode propagation ($0 - 1700 \omega_{pe}^{-1}$), (2) mode conversion ($1700 - 2100 \omega_{pe}^{-1}$), (3) Z mode reflection ($2100 - 2900 \omega_{pe}^{-1}$), (4) wave dissipation (after $2900 \omega_{pe}^{-1}$).

	frequency (kHz)	ω_{pe}/Ω_{ce}	Remarks on source location
Saturn	5 or 20	~ 5 for 20 kHz and ~ 0.8 for 5 kHz	Saturn's plasma torus at L shells 8 to 10 for 5 kHz NB and L4 to 7 for 20 kHz NB (Ye et al., 2009)
Jupiter	100-200	~ 10	mainly from the plasma disk within 5-25 R_J (Reiner et al., 1993; Imai et al., 2017; Boudouma et al., 2024)
Ganymede	15-60	~ 6	Near Magnetopause, $\sim 5.4 R_G$ (Kurth et al., 1997)
Earth	30-110	$\sim 3-10$	Plasmapause boundary layer (Grimald et al., 2008)

Table 1. Parameters of narrowband (NB) radiation from planetary magnetospheres.

Appendix A Linear theory and initial conditions

Equation (A1) presents the dispersion relation of cold plasma (Kalaee & Katoh, 2020). where n_{\parallel} and n_{\perp} denote the components of refractive index parallel and perpendicular to \vec{B}_0 . $\Gamma = [Y^4 \sin^4 \theta + 4(X-1)^2 Y^2 \cos^2 \theta]^{\frac{1}{2}}$, $X = \left(\frac{\omega_p}{\omega}\right)^2$, $Y = \frac{\omega_c}{\omega}$, where ω_c is the electron frequency, θ is the wave normal angle, and the $+$ ($-$) sign indicates the refractive index of the extraordinary (ordinary) mode. The ordinary and extraordinary modes coalesce when $\Gamma = 0$, requiring $X = 1$ and $\theta = 0$. Under these conditions, Equation (A1) simplifies to $n^2 = n_{\parallel}^2 = \frac{Y}{1+Y}$, indicating that mode conversion occurs at $\omega_p \sim \omega$ with $\theta = 0$ and $n_{\perp} = 0$. We calculated the plasma frequency at the reflection point (ω_r) for a given wave frequency (ω) using Equations 18 and 19 from Kalaee and Katoh (2020).

$$n^2 = n_{\parallel}^2 + n_{\perp}^2 = 1 - \frac{2X(X-1)}{2(X-1) - Y^2 \sin^2 \theta \pm \Gamma}. \quad (\text{A1})$$

Applying the Snell's law to Saturn's 20 kHz NB emission, we can derive the parameters of the to-be-pumped Z mode in the uniform region ($\omega = 5.03 \Omega_{ce}$) that are angle $\theta_0 = 70.6^\circ$ and $k_0 = 6.0 \Omega_{ce}/c$. By solving the dispersion relation and the Snell's law, we trace the Z mode propagation in the density gradient region (see Figure C1). As the Z mode propagates into denser region, θ decreases from 70° to $\sim 30^\circ$, then it reflects back into the dilute region with θ changing from 30° to -30° . Then θ approaches 0° causing the conversion of Z mode into O mode.

Appendix B Wave-pumping setup

Based on the linear cold plasma wave theory, we can determine the relative strengths of the six components of the electromagnetic field for any given mode with known parameters of ω , k , and θ (Ni et al., 2021). This prescribes the field components of the Z mode to-be-pumped, according to the following equations, where phase $\Phi = k \cdot \sin \theta \cdot x + k \cdot \cos \theta \cdot z$.

$$\vec{E} = E_x \sin(\Phi) \hat{e}_x + E_y \cos(\Phi) \hat{e}_y + E_z \sin(\Phi) \hat{e}_z, \quad (\text{B1})$$

$$\vec{B} = B_x \cos(\Phi) \hat{e}_x + B_y \sin(\Phi) \hat{e}_y + B_z \cos(\Phi) \hat{e}_z, \quad (\text{B2})$$

$$E_y = 0.0001, \quad (\text{B3})$$

$$E_x = \frac{(N^2 - S)}{D} \cdot E_y, \quad (\text{B4})$$

$$E_z = \frac{(S - N^2) \cdot (S - N^2 \cos^2 \theta)}{DN^2 \sin \theta \cos \theta} \cdot E_y, \quad (\text{B5})$$

$$B_x = -\frac{k \cos \theta}{\omega} \cdot E_y, \quad (\text{B6})$$

$$B_y = \left(\frac{k \cos \theta}{\omega} \cdot E_x - \frac{k \sin \theta}{\omega} \cdot E_z \right) \cdot E_y, \quad (\text{B7})$$

$$B_z = \frac{k \sin \theta}{\omega} \cdot E_y, \quad (\text{B8})$$

$$S = 1 - \frac{\omega_{pe}^2}{\omega^2 - \Omega_{ce}^2}, \quad (\text{B9})$$

$$N = \frac{kc}{\omega}, \quad (\text{B10})$$

$$D = -\frac{\Omega_{ce} \cdot \omega_{pe}^2}{\omega \cdot (\omega^2 - \Omega_{ce}^2)}. \quad (\text{B11})$$

Appendix C The method of mode identification and estimate of conversion efficiency

One can identify wave modes with dispersion diagrams given by the Fourier analysis (Chen et al., 2022; Zhang et al., 2023). Since the Z and O modes are close in dispersion diagrams at the condition of mode conversion, it is challenging to distinguish them according to the dispersion diagrams. Here, we do this by calculating the ratios of various electric field components according to the above expressions. The results are presented in Figure C2. The amplitudes of E_x and E_z of the Z mode decrease with decreasing θ . For quasi-parallel propagation, E_z of the O mode is stronger than that of the Z mode. Therefore, a significant enhancement of E_z indicates the presence of the O mode.

According to the linear theory, the O mode leaves the conversion regime at a quasi-parallel propagation, whereas the leftover Z mode leaves with a large propagation angle (see Figure C1). As shown by the dispersion curves (Figure C2), the O mode propagates much faster in group velocity than that of the Z mode. This means the dominance of the O mode in the uniform region shortly after the conversion. We calculated the electric field energies for Z mode (W_E^Z) and O mode (W_E^O) within the black-dashed region of Figure 3 to determine the rate of mode conversion ($\eta = (W_E^O) / (W_E^Z)$). As shown in Figure 3, a portion of the downward-propagating Z mode was reflected back into the domain, resulting in an enhancement of the E_x component in the uniform region. We excluded this enhanced component when calculating the mode energy.

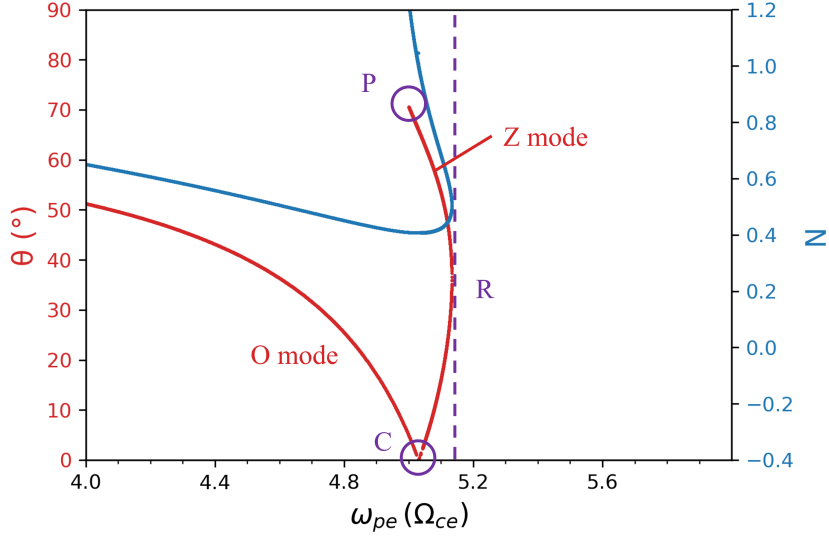


Figure C1. Ray-tracing of Z mode propagation in density gradient. X-axis: local electron plasma frequency normalized by electron gyro-frequency (Ω_{ce}). Curves show evolution of propagation angle θ (red line) and refractive index N (blue line). Labels: P (pumping), R (return), C (conversion).

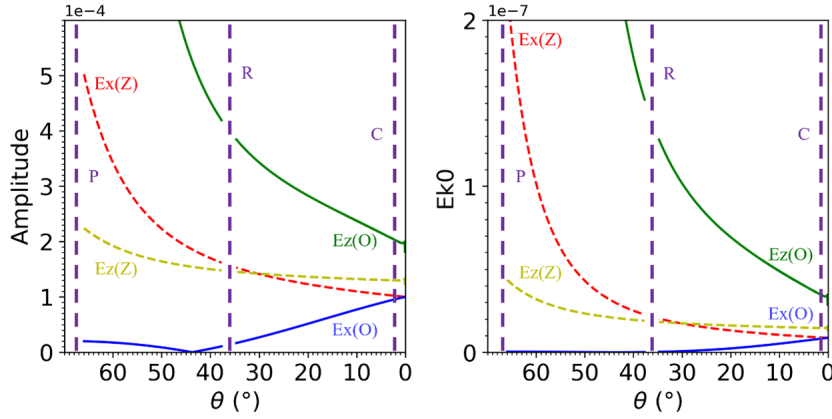


Figure C2. Amplitude (left) and energy (right) profiles of E_x and E_z components for Z mode (dashed) and O mode (solid) along the propagation path, calculated using cold-plasma theory. Data gaps correspond to the return zone. Labels: P (pumping), R (return), C (conversion).

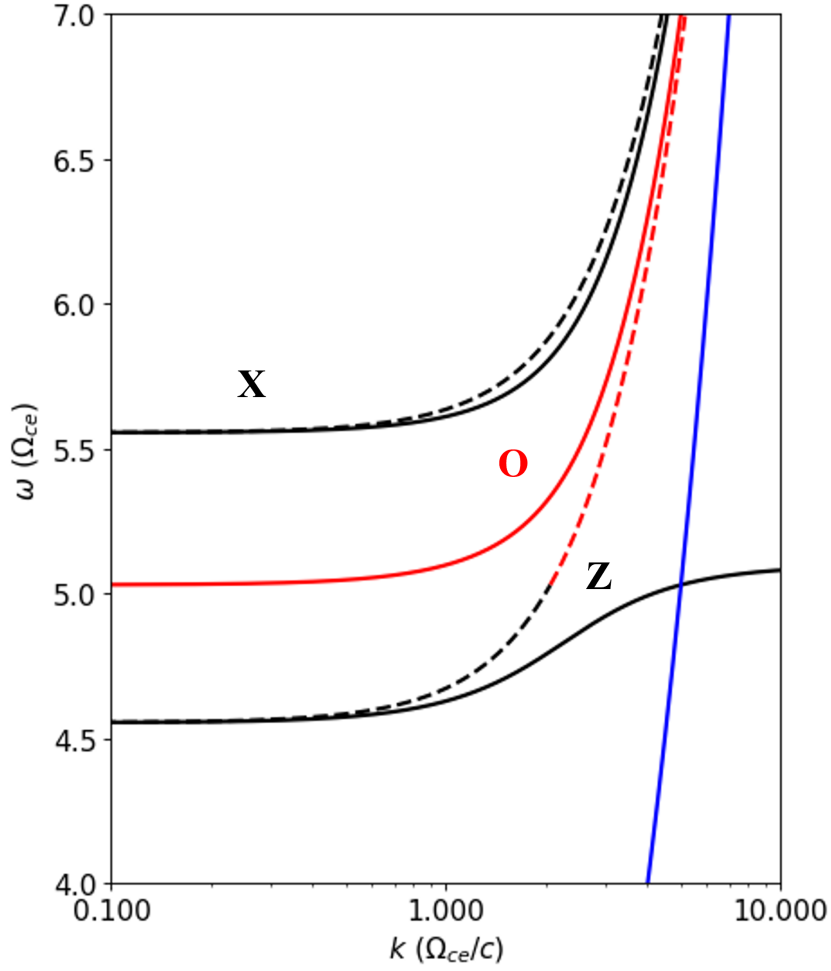


Figure C3. Theoretical dispersion relation at $\omega = 5.03 \Omega_{ce}$. The red black and blue lines mark O mode Z mode and light wave ($\omega = kc$). The solid and dashed lines represent $\theta = 70^\circ$ and $\theta = 0^\circ$, The slope of the curve gives the group velocity.

Open Research Section

All data necessary to validate the findings presented in this manuscript can be found by Mu (2024).

Acknowledgments

This study is supported by the National Natural Science Foundation of China (NNSFC) grants (Nos. 12103029, 12303061, 12203031), Shandong Provincial Natural Science Foundation (ZR2023QA141). The authors acknowledge the Beijing Super Cloud Computing Center (BSC-C, URL: <http://www.blsc.cn/>) for providing HPC resources, and the open-source Vector-PIC (VPIC) code provided by Los Alamos National Labs (LANL). We thank Professor Ye Shengyi for providing the observational data of Saturn's narrowband radiation, and Professors Lu Quanming and Li Gang for their constructive suggestions. We also appreciate Professor Yuto Katoh's assistance with the electron fluid model.

References

- Boudouma, A., Zarka, P., Louis, C. K., Briand, C., & Imai, M. (2024). Generation mechanism and beaming of jovian nkom from 3d numerical modeling of juno/waves observations. *Journal of Geophysical Research: Space Physics*, 129(4), e2023JA032280. doi: 10.1029/2023JA032280
- Bowers, K. J., Albright, B. J., Yin, L., Bergen, B., & Kwan, T. J. T. (2008). Ultra-high performance three-dimensional electromagnetic relativistic kinetic plasma simulation. *Physics of Plasmas*, 15(5), 055703. doi: 10.1063/1.2840133
- Bowers, K. J., Albright, B. J., Yin, L., Daughton, W., Roytershteyn, V., Bergen, B., & Kwan, T. J. T. (2009). Advances in petascale kinetic plasma simulation with vpik and roadrunner. *Journal of Physics: Conference Series*, 180, 012055. doi: 10.1088/1742-6596/180/1/012055
- Cairns, I. H., & Melrose, D. B. (1985). A theory for the $2 f_p$ radiation upstream of the earth's bow shock. *Journal of Geophysical Research: Space Physics*, 90(A7), 6637–6640. doi: 10.1029/JA090iA07p06637
- Chen, Y., Zhang, Z., Ni, S., Ning, H., Li, C., & Li, Y. (2022). Plasma emission induced by ring-distributed energetic electrons in overdense plasmas. *Physics of Plasmas*, 29(11), 112113. doi: 10.1063/5.0108780
- Décréau, P. M. E., Aoutou, S., Denazelle, A., Galkina, I., Rauch, J.-L., Vallières, X., ... Darrouzet, F. (2015). Wide-banded ntc radiation: Local to remote observations by the four cluster satellites. *Annales Geophysicae*, 33(10), 1285–1300. doi: 10.5194/angeo-33-1285-2015
- Ellis, G. (1956). The z propagation hole in the ionosphere. *Journal of Atmospheric and Terrestrial Physics*, 8(1-2), 43–54. doi: 10.1016/0021-9169(56)90090-3
- Ellis, G. R. A. (1962). Use of z-mode propagation for observing cosmic radio noise from earth satellites. *Nature*, 193(4818), 862–863. doi: 10.1038/193862a0
- Ginzburg, V. L., & Zhelezniakov, V. V. (1958). On the possible mechanisms of sporadic solar radio emission (radiation in an isotropic plasma). *Soviet Astronomy*, 2, 653.
- Grimald, S., Décréau, P. M. E., Canu, P., Rochel, A., & Vallières, X. (2008). Medium-latitude sources of plasmaspheric nonthermal continuum radiation observed close to harmonics of the electron gyrofrequency. *Journal of Geophysical Research: Space Physics*, 113(A11), 2008JA013290. doi: 10.1029/2008JA013290
- Grimald, S., & Santolík, O. (2010). Possible wave modes of wideband nonthermal continuum radiation in its source region. *Journal of Geophysical Research: Space Physics*, 115(A6), 2009JA014997. doi: 10.1029/2009JA014997
- Gurnett, D. A. (1975). The earth as a radio source: The nonthermal continuum. *Journal of Geophysical Research*, 80(19), 2751–2763. doi:

- 10.1029/JA080i019p02751
- Gurnett, D. A., Kurth, W. S., Roux, A., Bolton, S. J., & Kennel, C. F. (1996). Evidence for a magnetosphere at ganymede from plasma-wave observations by the galileo spacecraft. *Nature*, *384*(6609), 535–537. doi: 10.1038/384535a0
- Gurnett, D. A., Kurth, W. S., & Scarf, F. L. (1981). Narrowband electromagnetic emissions from saturn’s magnetosphere. *Nature*, *292*(5825), 733–737. doi: 10.1038/292733a0
- Gurnett, D. A., Kurth, W. S., & Scarf, F. L. (1983). Narrowband electromagnetic emissions from jupiter’s magnetosphere. *Nature*, *302*(5907), 385–388. doi: 10.1038/302385a0
- Henri, P., Sgattoni, A., Briand, C., Amiranoff, F., & Riconda, C. (2019). Electromagnetic simulations of solar radio emissions. *Journal of Geophysical Research: Space Physics*, *124*(3), 1475–1490. doi: 10.1029/2018JA025707
- Horký, M., & Omura, Y. (2019). Novel nonlinear mechanism of the generation of non-thermal continuum radiation. *Physics of Plasmas*, *26*(2), 022904. doi: 10.1063/1.5077094
- Horký, M., Omura, Y., & Santolík, O. (2018). Particle simulation of electromagnetic emissions from electrostatic instability driven by an electron ring beam on the density gradient. *Physics of Plasmas*, *25*(4), 042905. doi: 10.1063/1.5025912
- Imai, M., Kurth, W. S., Hospodarsky, G. B., Bolton, S. J., Connerney, J. E. P., & Levin, S. M. (2017). Direction-finding measurements of jovian low-frequency radio components by juno near perijove 1. *Geophysical Research Letters*, *44*(13), 6508–6516. doi: 10.1002/2017GL072850
- Jones, D. (1980). Latitudinal beaming of planetary radio emissions. *Nature*, *288*(5788), 225–229. doi: 10.1038/288225a0
- Jones, D. (1987). The magnetopause as a source of nonthermal continuum radiation. *Physica Scripta*, *35*(6), 887–894. doi: 10.1088/0031-8949/35/6/022
- Kaiser, M. L., Desch, M. D., Farrell, W. M., MacDowall, R. J., Stone, R. G., Lecacheux, A., ... Zarka, P. (1992). Ulysses observations of escaping vlf emissions from jupiter. *Geophysical Research Letters*, *19*(7), 649–652. doi: 10.1029/92GL00387
- Kalaee, M. J., & Katoh, Y. (2014). A simulation study on the mode conversion process from slow z-mode to lo mode by the tunneling effect and variations of beaming angle. *Advances in Space Research*, *54*(11), 2218–2223. doi: 10.1016/j.asr.2014.08.025
- Kalaee, M. J., & Katoh, Y. (2020). Plasma frequency demand for mode conversion processes from slow z-mode to lo-mode waves in an inhomogeneous plasma. *Earth, Planets and Space*, *72*(1), 95. doi: 10.1186/s40623-020-01226-x
- Kalaee, M. J., Ono, T., Katoh, Y., Iizima, M., & Nishimura, Y. (2009). Simulation of mode conversion from uhr-mode wave to lo-mode wave in an inhomogeneous plasma with different wave normal angles. *Earth, Planets and Space*, *61*(11), 1243–1254. doi: 10.1186/BF03352977
- Kim, E.-H., Cairns, I. H., & Robinson, P. A. (2007). Extraordinary-mode radiation produced by linear-mode conversion of langmuir waves. *Physical Review Letters*, *99*(1), 015003. doi: 10.1103/PhysRevLett.99.015003
- Kim, E.-H., Cairns, I. H., & Robinson, P. A. (2008). Mode conversion of langmuir to electromagnetic waves at magnetic field-aligned density inhomogeneities: Simulations, theory, and applications to the solar wind and the corona. *Physics of Plasmas*, *15*(10), 102110. doi: 10.1063/1.2994719
- Krafft, C., & Savoini, P. (2021). Second harmonic electromagnetic emissions by an electron beam in solar wind plasmas with density fluctuations. *The Astrophysical Journal Letters*, *917*(2), L23. doi: 10.3847/2041-8213/ac1795
- Krafft, C., & Savoini, P. (2024). Electrostatic wave decay in the randomly inhomogeneous solar wind. *The Astrophysical Journal Letters*, *964*(2), L30. doi: 10.3847/2041-8213/ad3449

- Krafft, C., Savoini, P., & Polanco-Rodríguez, F. J. (2024). Mechanisms of fundamental electromagnetic wave radiation in the solar wind. *The Astrophysical Journal Letters*, *967*(2), L20. doi: 10.3847/2041-8213/ad47b5
- Krafft, C., & Volokitin, A. S. (2024). Second harmonic electromagnetic wave emissions from a turbulent plasma with random density fluctuations. *The Astrophysical Journal*, *964*(1), 65. doi: 10.3847/1538-4357/ad20ee
- Kurth, W. S., Gurnett, D. A., & Anderson, R. R. (1981). Escaping nonthermal continuum radiation. *Journal of Geophysical Research: Space Physics*, *86*(A7), 5519–5531. doi: 10.1029/JA086iA07p05519
- Kurth, W. S., Gurnett, D. A., Roux, A., & Bolton, S. J. (1997). Ganymede: A new radio source. *Geophysical Research Letters*, *24*(17), 2167–2170. doi: 10.1029/97GL02249
- Kurth, W. S., Sulaiman, A. H., Hospodarsky, G. B., Menietti, J. D., Mauk, B. H., Clark, G., ... Louis, C. (2022). Juno plasma wave observations at ganymede. *Geophysical Research Letters*, *49*(23), e2022GL098591. doi: 10.1029/2022GL098591
- Melrose, D. B. (1980). The emission mechanisms for solar radio bursts. *Space Science Reviews*, *26*, 3–38. doi: 10.1007/BF00212597
- Menietti, J. D., Shprits, Y. Y., Horne, R. B., Woodfield, E. E., Hospodarsky, G. B., & Gurnett, D. A. (2012). Chorus, ech, and z mode emissions observed at jupiter and saturn and possible electron acceleration. *Journal of Geophysical Research: Space Physics*, *117*(A12), 2012JA018187. doi: 10.1029/2012JA018187
- Menietti, J. D., Ye, S.-Y., Yoon, P. H., Santolik, O., Rymer, A. M., Gurnett, D. A., & Coates, A. J. (2009). Analysis of narrowband emission observed in the saturn magnetosphere. *Journal of Geophysical Research: Space Physics*, *114*(A6), 2008JA013982. doi: 10.1029/2008JA013982
- Menietti, J. D., Yoon, P. H., Pisa, D., Averkamp, T. F., Sulaiman, A. H., Kurth, W. S., ... Arridge, C. S. (2019). The role of intense upper hybrid resonance emissions in the generation of saturn narrowband emission. *Journal of Geophysical Research: Space Physics*, *124*(7), 5709–5718. doi: 10.1029/2019JA026855
- Mu, Z. (2024). *Data for PIC simulation on mode conversion of Saturn's 20 kHz narrowband radio emission* [Dataset]. Zenodo. doi: 10.5281/zenodo.14511249
- Ni, S., Chen, Y., Li, C., Sun, J., Ning, H., & Zhang, Z. (2021). An alternative form of the fundamental plasma emission through the coalescence of z-mode waves with whistlers. *Physics of Plasmas*, *28*(4), 040701. doi: 10.1063/5.0045546
- Reiner, M. J., Fainberg, J., Stone, R. G., Kaiser, M. L., Desch, M. D., Manning, R., ... Pedersen, B.-M. (1993). Source characteristics of jovian narrow-band kilometric radio emissions. *Journal of Geophysical Research: Planets*, *98*(E7), 13163–13176. doi: 10.1029/93JE00536
- Robinson, P. A., Cairns, I. H., & Willes, A. J. (1994a). Dynamics and efficiency of type iii solar radio emission. *The Astrophysical Journal*, *422*, 870. doi: 10.1086/173779
- Robinson, P. A., Cairns, I. H., & Willes, A. J. (1994b). Dynamics and efficiency of type iii solar radio emission. *The Astrophysical Journal*, *422*, 870. doi: 10.1086/173779
- Sakai, J. I., Mori, T., & Saito, S. (2005). Simulation on solar type ii radio bursts associated with corona mass ejections. *Astronomy & Astrophysics*, *442*(2), 687–692. doi: 10.1051/0004-6361:20053033
- Thurgood, J. O., & Tsiklauri, D. (2015). Self-consistent particle-in-cell simulations of fundamental and harmonic plasma radio emission mechanisms. *Astronomy & Astrophysics*, *584*, A83. doi: 10.1051/0004-6361/201527079
- Willes, A. J., & Cairns, I. H. (2001). Mode conversion and reflection of langmuir waves in an inhomogeneous solar wind. *Publications of the Astronomical Soci-*

- ety of Australia*, 18(4), 355–360. doi: 10.1071/AS01051
- Wu, S., Ye, S., Fischer, G., Wang, J., Long, M., Menietti, J. D., ... Kurth, W. S. (2021). Statistical study on spatial distribution and polarization of saturn narrowband emissions. *The Astrophysical Journal*, 918(2), 64. doi: 10.3847/1538-4357/ac0af1
- Ye, S.-Y., Gurnett, D. A., Fischer, G., Cecconi, B., Menietti, J. D., Kurth, W. S., ... Lecacheux, A. (2009). Source locations of narrowband radio emissions detected at saturn. *Journal of Geophysical Research: Space Physics*, 114(A6), 2008JA013855. doi: 10.1029/2008JA013855
- Ye, S.-Y., Menietti, J. D., Fischer, G., Wang, Z., Cecconi, B., Gurnett, D. A., & Kurth, W. S. (2010). Z mode waves as the source of saturn narrowband radio emissions. *Journal of Geophysical Research: Space Physics*, 115(A8), 2009JA015167. doi: 10.1029/2009JA015167
- Zhang, Z., Chen, Y., Li, C., Ni, S., Ning, H., Li, Y., ... Kong, X. (2023). Waves and plasma emissions excited by ring-beam energetic electrons interacting with weakly magnetized plasmas. *Physics of Plasmas*, 30(12), 122106. doi: 10.1063/5.0175997
- Zhang, Z., Chen, Y., Ni, S., Li, C., Ning, H., Li, Y., & Kong, X. (2022). Verification of the standard theory of plasma emission with particle-in-cell simulations. *The Astrophysical Journal*, 939(2), 63. doi: 10.3847/1538-4357/ac94c6